

Article

Magneto-Transport and Enhanced Spin-Polarized Photo Response in Solution-Processed Vertically Aligned Zn_{0.9}Ni_{0.1}O Nanowires

Jamil Kazmi ^{1,2,†}, Jamal Kazmi ^{2,*,†} , Syed Raza Ali Raza ^{3,*}, Babar Nazir ¹, Raja Azhar Saeed Khan ^{1,4}, Mohd Ambri Mohamed ²  and Mohsin Rafique ^{5,*} 

¹ Department of Physics, The University of Azad Jammu and Kashmir, Muzaffarabad 13100, Azad Kashmir, Pakistan

² Institute of Microengineering and Nanoelectronics (IMEN), Universiti Kebangsaan Malaysia (UKM), Bangi 43600, Selangor, Malaysia

³ Department of Physics, Allama Iqbal Open University, Islamabad 44000, Pakistan

⁴ Department of Physics, Women University of Azad Jammu & Kashmir, Bagh 12500, Azad Kashmir, Pakistan

⁵ Beijing Academy of Quantum Information Sciences, Beijing 100193, China

* Correspondence: jamal_physics@outlook.com (J.K.); raza_physics@hotmail.com (S.R.A.R.); mmohsin8389@gmail.com (M.R.)

† These authors contributed equally to this work.

Abstract: In this study, we grew pristine and Ni-doped vertically aligned zinc oxide nanowires (NWs) on a glass substrate. Both the doped and pristine NWs displayed dominant 002 peaks, confirming their vertical alignment. The Ni-doped NWs exhibited a leftward shift compared to the pristine NWs. TEM measurements confirmed the high crystallinity of individual NWs, with a d-spacing of ~0.267 nm along the c-axis. Ni-doped NWs had a higher density, indicating increased nucleation sites due to nickel doping. Doped NW films on glass showed enhanced absorbance in the visible region, suggesting the creation of sub-gap defect levels from nickel doping. Magnetization vs. magnetic field measurements revealed a small hysteresis loop, indicative of soft ferromagnetic behavior. Current transient plots demonstrated an increase in current with an applied magnetic field. Two-terminal devices exhibited a photo response that intensified with magnetic field application. This increase was attributed to parallel grain alignment, resulting in enhanced carrier concentration and photo response. In the dark, transport properties displayed negative magnetoresistance behavior. This magneto-transport effect and enhanced photo response (under an LED at ~395 nm) were attributed to giant magnetoresistance (GMR) in the aligned NWs. The observed behavior arose from reduced carrier scattering, improved transport properties, and parallel spin alignment in the magnetic field.

Keywords: diluted magnetic semiconductors; spintronics; solution synthesis; UV detector; magnetoresistance



Citation: Kazmi, J.; Kazmi, J.; Raza, S.R.A.; Nazir, B.; Khan, R.A.S.; Mohamed, M.A.; Rafique, M. Magneto-Transport and Enhanced Spin-Polarized Photo Response in Solution-Processed Vertically Aligned Zn_{0.9}Ni_{0.1}O Nanowires. *Magnetochemistry* **2023**, *9*, 193. <https://doi.org/10.3390/magnetochemistry9080193>

Academic Editors: Lucian Petrescu and Catalin Constantinescu

Received: 28 June 2023

Revised: 17 July 2023

Accepted: 19 July 2023

Published: 26 July 2023



Copyright: © 2023 by the authors. Licensee MDPI, Basel, Switzerland. This article is an open access article distributed under the terms and conditions of the Creative Commons Attribution (CC BY) license (<https://creativecommons.org/licenses/by/4.0/>).

1. Introduction

Spintronics, which harnesses both the charge and spin of electrons, has emerged as a promising field for next-generation electronic and information-processing devices. While various materials have been explored for spintronic applications, it is crucial to highlight the unique advantages offered by ZnO films [1–3]. Firstly, ZnO is a direct wide-bandgap semiconductor, making it well-suited for efficient charge carrier injection and transport in spintronic devices. Moreover, ZnO exhibits remarkable optical properties, particularly at short wavelengths, making it suitable for integration with optical functionalities in spintronic circuits [4].

Compared to traditional spintronic materials such as YIG, ZnO films present several distinct advantages. YIG is primarily utilized for its long spin relaxation times and low Gilbert damping, which are advantageous for spin transport. However, YIG typically

requires complex fabrication processes and integration schemes to interface with other materials, limiting its compatibility and scalability in device fabrication [5]. On the other hand, ZnO films can be grown using various deposition techniques, including pulsed laser deposition, chemical vapor deposition, and molecular beam epitaxy, enabling flexible and scalable fabrication processes with well-controlled film properties.

Adding a spin degree of freedom in semiconductors is highly desired for multifunctional devices [6]. It can be achieved by doping magnetic ions in the host semiconductors, which leads to an exchange interaction between the itinerant sp-band electrons or holes and the d-electron spins localized at the dopant ions. This exclusive approach has manifested in diluted magnetic semiconductors (DMS) design. The DMS devices offer certain advantages [6], including non-volatility, enhanced processing speed, high energy efficiency, and increased integration densities. ZnO-based DMS systems have drawn tremendous attention because of their pronounced optical properties at short wavelengths and robust magnetic properties at room temperature, making them suitable for applications in electronics and spintronics [7,8]. For device applications, the Curie temperature up to or at least at room temperature is highly desired [9–11] to realize technological applications [12,13].

First-principles calculations [6] have predicted that when ZnO is doped with transitional metal dopants (V, Cr, Fe, Co, Ni), ferromagnetic order can be achieved as these dopants can produce a partially filled spin-split impurity band. Experimentally, ferromagnetic order with a Curie temperature higher than 300 K has also been reported for Mn [6], Fe [14], Co and Fe-(codoped) [15], and Ni-doped [16] ZnO DMS. The Ni-doped ZnO (Ni-ZnO) is considered a promising DMS system, where its optical properties (band gap ~3.3 eV, exciton binding energy combined with room-temperature ferromagnetic order due to Ni, make it an attractive candidate for potential monolithic optical integrated circuit applications in a short-wavelength field. However, the preparation of Ni-ZnO is challenging due to a significant driving force for phase segregation into NiO and ZnO; consequently, only a few studies have been reported until now. Wakano et al. [17] reported ferromagnetism below 30 K in Ni-doped films grown by pulsed laser deposition. Singh et al. [18] reported ferromagnetism with Curie temperature above 300 K in films grown by the sol-gel technique. In the PLD-grown ZnO films, Liu et al. [16] reported an intrinsic ferromagnetism that decreased with Ni-doping. Variations in the microstructure related to the growth techniques could be a reason for different magnetic properties, wire geometry, and density [19]. To further delve into the structural properties of ZnO-based films, recent studies have explored advanced characterization techniques. There are numerous reports both on theoretical and experimental approaches exploring the optical, optical, structural and magnetic properties of ZnO [20–23]. For instance, Guermat et al. (2021) employed high-resolution transmission electron microscopy (HRTEM) to investigate the crystal structure and morphology of ZnO films [24]. Their findings revealed well-defined wurtzite phase structures with a precise control over the film thickness. In addition, the study by Tiwari et al. (2022) employed X-ray diffraction (XRD) analysis to examine the lattice parameters and crystal quality of ZnO-based films grown via a chemical vapor deposition (CVD) method, demonstrating highly crystalline films with a preferred orientation along the (002) plane [25].

Investigating the optical properties of ZnO-based films, recent research has focused on understanding their bandgap energies and light absorption capabilities. A study by Soumya et al. (2023) investigated the bandgap engineering of ZnO films through precise doping strategies [26]. By varying the doping concentrations of transition metal ions, they observed a redshift in the optical absorption spectra, demonstrating the tunability of bandgap energies in ZnO-based films. Furthermore, Benhaliliba et al. (2021) utilized spectroscopic ellipsometry to study the optical absorption properties of ZnO-based films [27]. Their research revealed an enhanced light absorption in the ultraviolet (UV) region, attributed to the presence of defect states and surface plasmon resonance effects.

These recent studies highlight the advancements in understanding the structural and optical properties of ZnO-based films. By incorporating these findings, our manuscript

aims to contribute to the existing knowledge by providing a comprehensive overview of the important characteristics of ZnO-based films, including their crystal structure, morphology, and optical properties.

In this paper, we studied the structural, magnetic, magneto-optical, and magneto-transport properties (at room temperature) of Ni-doped ZnO NWs. The Ni-doping in ZnO imparts magnetic response, a red shift in the optical band gap, and negative magnetoresistance. In the presence of an external magnetic field, the localized magnetic moments align in the direction of the field, reduce the scattering of the carriers, and give rise to a negative magnetoresistance.

2. Materials and Methods

Chemicals: Analytical reagents zinc acetate dehydrates (ZnA), Zn (CH₃COO), and NaOH were used as precursor sources for the preparation of ZnO nanoparticles (NPs). The hexamethylenetetramine (HMTA) C₆H₁₂N₄ and zinc nitrate hexahydrate (ZnN) Zn(NO₃)₂·6H₂O were used to grow the ZnO NWs. Nickel nitrate hexahydrate Ni(NO₃)₂·6H₂O was added as a dopant in ZnO NWs. All mentioned materials were purchased from Sigma Aldrich (St. Louis, MO, USA) and used without further purification.

Synthesis of ZnO NWs Films: Pure and Ni-doped ZnO NWs were hydrothermally grown on seeded glass or Si substrates. Using a magnetic stirrer, 0.01 M of ZnA weighing 43.87 mg was dissolved in 20 mL of methanol and stirred at 60 °C for 30 min on a hot plate. A 0.09 M NaOH solution weighing 72 mg was produced in 20 mL of methanol and stirred at room temperature for 30 min. To keep the temperature of the ZnA solution constant, a reducing agent called NaOH solution was heated at 60 °C for 5–7 min. Afterwards, the NaOH solution was added dropwise to the ZnA solution which was stirred with a stirrer with a magnetic stirrer at 60 °C for 2 h to prepare the stabilized ZnO NPs. The synthesis of these ZnO nanoparticles or nanoseeds is schematically described in steps in the electronic Supplementary Information (ESI) Figure S1. The cleaned Si and glass substrates were spin-coated with the ZnO nanoparticle suspension solution. Using acetone, ethanol, and distilled water (DI water), in that order, both substrates were cleaned ultrasonically for 12 min each. Following coating, the substrates were annealed in a furnace at 300 °C. Then, an equimolar solution of ZnN and HMTA in DI water was created and stirred for two h at room temperature to create a homogenous solution. The substrates coated with ZnO nanoseeds were positioned upside down in the beaker containing the precursor solution. Afterwards, the beaker was wrapped in aluminum foil and put in a convection oven that was kept at 95 °C for 6 to 8 h. In the solution, HMTA released OH[−] ions, which built up on the positive polarity sidewalls of ZnO NWs and prevent sidewall growth while promoting vertical growth solely. The same HMTA and zinc nitrate solution were used for Ni-doping, and equimolar nickel nitrate hexahydrate was added to the ZnN solution. In order to remove any organic contaminants and enhance the crystal quality of ZnO NWs, the substrates were taken out of the solution, washed with DI water, and annealed at ambient conditions under an argon flow at 350 °C for 30 min in the furnace.

Morphological and Structural properties: The morphology of the samples was analyzed by scanning electron microscope (SEM), while the structural studies were carried out using an X-ray diffraction (XRD) D8 Bruker advanced X-ray diffractometer with a Cu k radiation ($\lambda = 1.54$ Å) and a transmission electron microscope (TEM, ZEISS); we were able to analyze the sample's crystal structure and growth direction.

Optical Characterizations: A twin-beam UV-visible spectrometer employing the Hitachi U-3900H, Berlin, Germany (measurement taken at Department of Physics, The University of Azad Jammu and Kashmir, Muzaffarabad-13100, Azad Kashmir, Pakistan) was used to record the optical absorption spectra of the samples in the 250–800 nm range. At room temperature, photoluminescence (PL) spectra of the samples were taken using a 5 mW He-Cd laser with an excitation wavelength of 325 nm. A 60-second laser exposure time was chosen. It was decided to use a diffraction grating with 1200 lines/mm for the PL measurements. The elemental content and oxidation state of the produced samples

were determined using X-ray photoelectron spectroscopy (XPS) on a ULVAC Quantera II, Tokyo, Japan (measurements taken at MIMOS, Malaysia) with an Alk monochromatic source (1486.6 eV).

Magnetic Studies: A superconducting quantum interference device (SQUID) magnetometer (model: M355 Quantum Design, Inc., New York, NY, USA) was used to measure the DC magnetization for a range of temperatures down to 4 K and magnetic fields up to 50,000 Oe.

Device Fabrication and Magneto-transport Measurement: A two-terminal device was fabricated with aluminum foil as a metal electrode attached to ZnO NW film on the glass substrate; the length of the device, i.e., electrode spacing, was ~2 mm and its width was 7 mm. The substrate was put on a neodymium permanent magnet with a strength of ~0.2 T for the electrical characterization in the dark and under the illumination of a UV (395 nm) LED with and without the application of a magnetic field. The Al contacts were attached tightly using scotch tape, and the electrodes were connected to a Keithley 2400, Beijing, China (measurement taken at Department of Physics, The University of Azad Jammu and Kashmir, Muzaffarabad-13100, Azad Kashmir, Pakistan) source meter through crocodile clip wires.

3. Results and Discussion

Through a series of comprehensive characterizations and measurements, we explored the structural, magnetic, and magneto-transport behavior of the nanowires. Our study aimed to shed light on the influence of Ni doping on the properties of ZnO nanowires, particularly focusing on the manifestation of soft magnetic behavior and its implications for potential spintronic applications. We begin by discussing the structural analysis, highlighting the morphology and crystalline structure of the nanowires. Subsequently, we delve into the magnetic properties, elucidating the room-temperature ferromagnetic behavior observed in the Ni-doped ZnO nanowires. Furthermore, we present the magneto-transport measurements, showcasing the negative magnetoresistance and its correlation with the magnetic behavior. The comprehensive analysis in this section contributes to our understanding of the unique properties of Ni-doped ZnO nanowires, opening avenues for their potential applications in spintronics and magnetic devices.

Figure 1 shows the surface morphology of the grown nanowires studied by using SEM. Figure 1a shows pure ZnO NWs while Figure 1b shows Ni-doped ZnO NWs grown on a glass substrate. It is observed that after Ni-doping, the nanowires have become denser as well as vertically aligned compared to pure ZnO NWs. Thus, it can be suggested that Ni doping results in an improved vertical alignment. The doping of transition-metal ions can dramatically affect the microstructure. In Figure 1c, a high-resolution image shows the top view of vertically grown Ni-ZnO NWs on a glass substrate; hexagonal top facets can be observed. The frequency distribution diagram of the Ni-ZnO NWs is shown in Figure 2d, which yields an average diameter (with a lognormal fit) of ~322.7 nm, while in our previous reports, we observed that the average diameter of pure ZnO NWs was about ~86 nm [10,28].

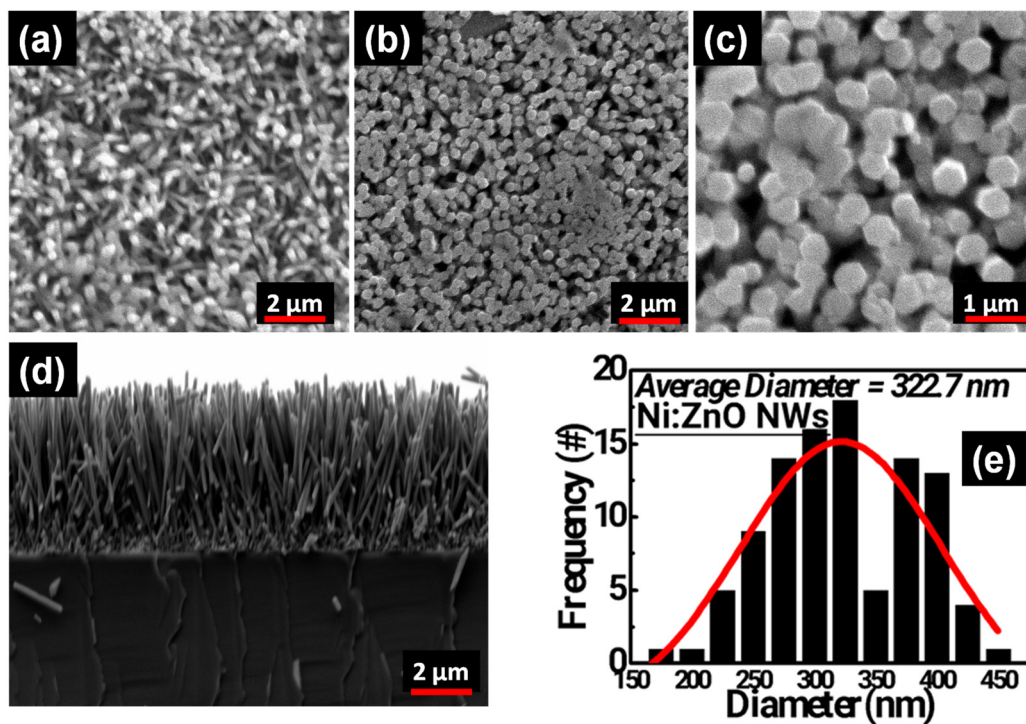


Figure 1. Surface morphology of nanowires grown on glass substrate by using a wet chemical synthesis; (a) pure ZnO NWs; (b) Ni-ZnO NWs; (c) high-resolution image showing the top view (hexagonal) of NWs; (d) SEM cross-section image of ZnO NWs grown on a silicon substrate under the same conditions as these on the glass substrate; (e) frequency distribution graph of Ni-ZnO NWs.

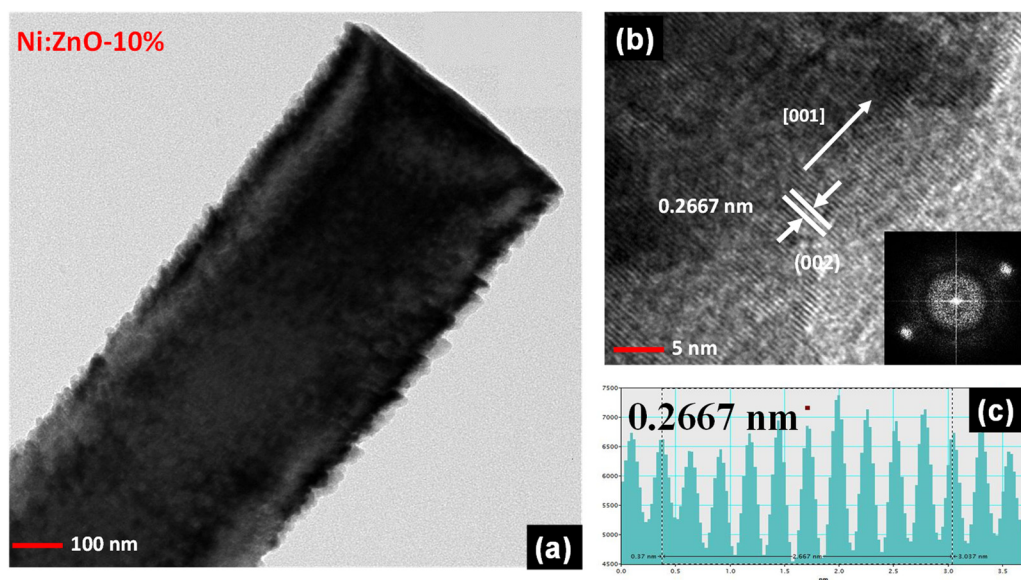
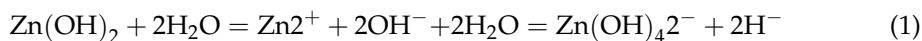
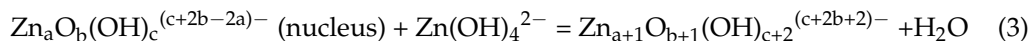


Figure 2. Microstructure of a single Ni-ZnO nanowire (a) TEM image, and (b) HRTEM image with inset showing the diffraction pattern. (c) Diffraction spectra from HRTEM measurements.

The vertical growth of nickel-doped ZnO NWs by the hydrothermal method is explained as follows. The Zn(OH)₂ gel dissolves into the OH⁻ ion-supersaturated solution. It draws ions and creates a growth unit, as seen below:

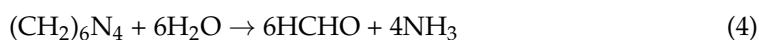


Then, because of the heat convection, the ions spread, and the movement of ions and molecules declines. The dehydration of the growth units leads to the formation of $Zn_aO_b(OH)_c^{(c+2b2a)-}$ clusters. The ZnO nucleus is produced as shown in Equations (2) and (3) as the particle size of the cluster $Zn_aO_b(OH)_c^{(c+2b2a)-}$ gets closer to a particular value.



The number of Zn^{2+} , O^- , and OH^- atoms in the crystal are indicated by the subscripts a, b, and c in the abovementioned equations. The ZnO formation mechanism makes it clear that the dehydration of the OH^- ligands results in the growth unit's incorporation into the crystal lattice [29]. Because of the OH^- ligands on the interfaces, the ZnO crystal formation is related to them. Every time a hydrothermal reaction occurs in a different solution, a piece of the OH^- ligands on the surface of the clusters $Zn_aO_b(OH)_c^{(c+2b2a)-}$ may be protected by other ions in the medium, creating a cationic interface with the water or other ions present in the structure. As a result, the crystal's development pattern is closely related to the reaction media. The impact of the external conditions at the interfaces on the OH^- ligands is low when we have a neutral medium. Thus, the interior structure has a significant impact on the crystal habit. Out of all the crystal faces, the (001) face grows the quickest. The OH^- ions concentration that HMTA ejected decreases when the Ni concentration is raised. The NWs develop radially as a result of these diminished OH^- ions. The thermodynamic barrier that is created when Ni is added to ZnO reduces both the nucleation process and the growth of the primary nuclei. The modest alteration in the structure of NWs can be attributed to the possibility that the Ni may produce a type of hydroxide complex during the growth process that hinders the reaction between OH^- and Zn^{2+} and changes the nucleation development as a whole. Instead of causing a vertical expansion, this process may drive a horizontal growth. NWs become larger as a result [30]. The following describes a potential reaction process for the deposition of ZnO from $Zn(NO_3)_2$ and the HMTA precursors at 65 °C.

Here, HMTA breaks down when heated into formaldehyde and ammonia, as shown in Equation (4). Ammonia and water interact in the second stage, as depicted in Equation (5). The insoluble ZnO then crystallizes as a result of this process (Equations (6) and (7)). When a substrate is added to the mixture, it precipitates both non-uniformly and uniformly. According to our research, $Zn(OH)_2$ may develop before ZnO growth. Then, it spreads through a mechanism of dissolution and re-precipitation, with $Zn(OH)_2$ acting as a zinc reservoir. The pH of the solution, which the HMTA ions supply, causes ZnO to be produced as a final product. The ZnO morphology is very much dependent on the experimental conditions, particularly the Zn^{2+} ions that alter the rate at which the hydroxylation occurs, as shown in Equations (6) and (7), allowing ZnO to modify its growth pattern. The dehydration reaction primarily uses the precursor solution with a low Zn^{2+} content. Therefore, once $Zn(OH)_2$ is created, it might be changed into ZnO. Consequently, $Zn(OH)_2$ might be changed to ZnO after being created. Due to the anisotropic growth of the hexagonal wurtzite structure in the (0001) direction, it results in the development of 1D ZnO NWs, as seen in SEM images Figure 2a–c.



Because the hydroxylation reaction proceeds relatively more quickly due to the high concentration of Zn^{2+} ions, the $Zn(OH)_2$ dehydration is delayed as the number of precursors increases. Two-dimensional structures may result as a result of this. Because of this, the

quantity of Zn^{2+} ions produced as a result of the precursors will also grow at very high precursor concentrations. The growth of nanostructures becomes extremely dense because of the increased nucleation sites and aggregation. It can be seen that the density of NWs in the Ni-doped sample is large as compared to the pristine NWs, as shown in Figure 1a–c. This occurred because of the precipitation of extra Ni atoms during the formation of NWs. This phenomenon suggests that when doping Ni in ZnO NWs, the NWs' density and aspect ratio increase. The high doping of nickel (10%) creates more nucleation sites, resulting in the dense growth of NWs, as evident from Figure 1a–c.

The microstructure of a single Ni-ZnO nanowire detached from the substrate was studied and is shown in Figure 2. In contrast to the phase segregation or clusters reported in the literature, the Ni incorporated in the ZnO matrix. The interlayer spacing was ~ 0.267 nm, as shown in the HRTEM image in Figure 2b, which was comparable with our previous report, where a TEM analysis yielded an interlayer spacing of 0.26 nm for pure ZnO NWs [10,11,31,32]. A slight difference in interlayer spacing of Ni-ZnO compared with ZnO NWs is due to the slight difference of ionic radii of Ni^{2+} (1.36 Å) and Zn^{2+} (0.74 Å), leading to a strain in ZnO matrix. The clear lattice fringes indicate a high-quality crystal structure of ZnO NW with a uniform surface area along the c-axis in the direction of the (002) plane. Producing such a high crystalline structure using a simple solution process is very desirable for device.

The XRD spectra of pure and Ni-ZnO NWs shown in Figure 3 revealed a hexagonal crystal structure for both pure and doped ZnO NWs. The observed peaks confirmed the formation of the wurtzite crystal structure of ZnO and the growth of NWs with a high crystallinity along the c-axis. The θ - 2θ scans showed no detectable impurity phases in the ZnO matrix. Due to the difference in the size of ionic radii of Ni^{2+} and Zn^{2+} , a lattice distortion was observed in the Ni-ZnO NWs. Bragg's law and Debye Scherrer formula [11,33–36] were used to calculate the structural parameters and crystalline size. The crystallite sizes from the FWHM for the 002 peaks were ~ 61 nm and ~ 116 nm, respectively, for the ZnO and Ni-ZnO NWs film on a glass substrate.

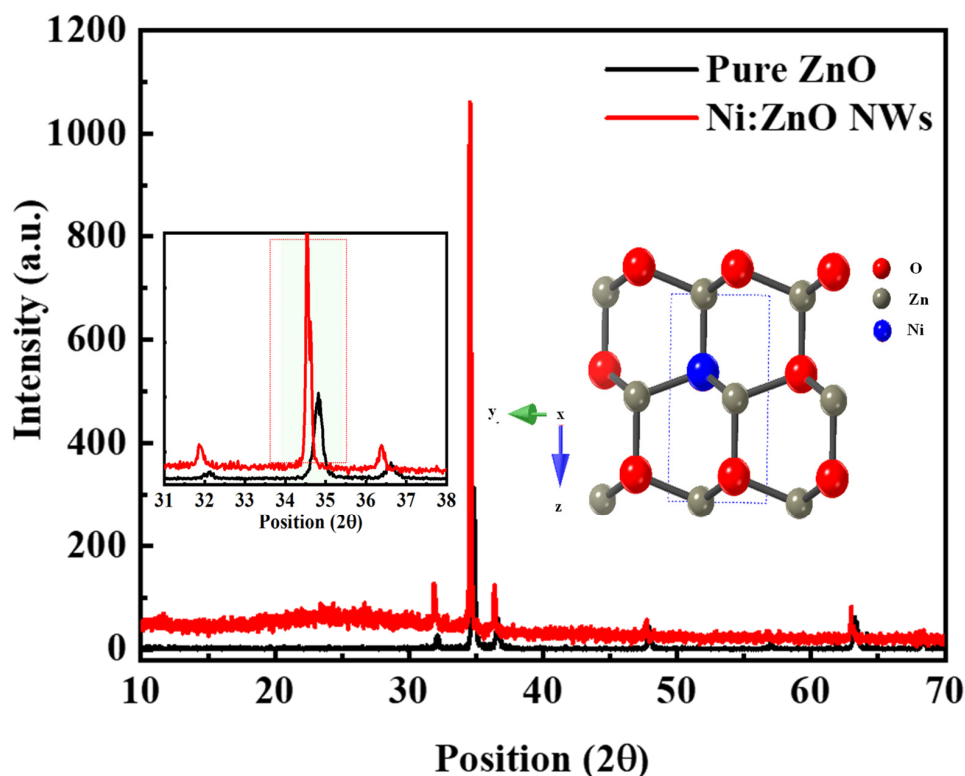


Figure 3. X-ray diffraction θ - 2θ pattern for ZnO and Ni-ZnO NWs on the glass substrate.

The UV–visible absorbance vs. wavelength spectra of the pure and Ni-ZnO NWs films on glass substrates is shown in Figure 4a. The doped films have an enhanced absorbance in the visible region, indicating the introduction of sub-gap defect levels due to doping, causing the sub-bandgap absorbance [37]. The $(\alpha h\nu)^2$ vs. energy Tauc plot for a direct-bandgap semiconductor for pure and Ni-doped ZnO NW films on a glass substrate is shown in Figure 4b. The absorbance edge is observed to be redshifted for the doped samples. The absorption edge for the pure and Ni-doped ZnO NWs film came out to be 2.96 eV and 1.94 eV, respectively. The red shift is most probably due to the introduction of sub-gap defect states due to doping. This also indicates the incorporation of Ni in the host lattice of ZnO. Ni-doping has also been reported in the literature to decrease the band gap of the ZnO [38–40]. Since the doping has red-shifted the absorption edge, the band gap of the films was calculated using the following Tauc’s equation:

$$\alpha h\nu = A(h\nu - E_g)^{\frac{1}{2}} \quad (8)$$

$$\ln(\alpha h\nu) = \ln A + \frac{1}{2} \ln(h\nu - E_g)^{-} \quad (9)$$

$$\frac{d[\ln(\alpha h\nu)]}{d[h\nu]} = \frac{1}{2(h\nu - E_g)} \quad (10)$$

Here α is the absorption coefficient ($=2.303 \frac{\text{Absorbance}}{\text{Thickness of film}}$), E_g , is energy bandgap. Therefore, after plotting a graph between $\frac{d[\ln(\alpha h\nu)]}{d[h\nu]}$ and $h\nu$, there must be a discontinuity at $h\nu = E_g$. This derivative plot is shown in Figure 4c, where the energy gap for the pure film is 3.27 eV, and that of Ni-10%:ZnO was calculated as 3.22 eV. Consequently, the bandgap has been reduced due to the Ni doping, which is quite understandable as the Ni-doping might have introduced the deep or shallow sub-gap states responsible for this band gap reduction.

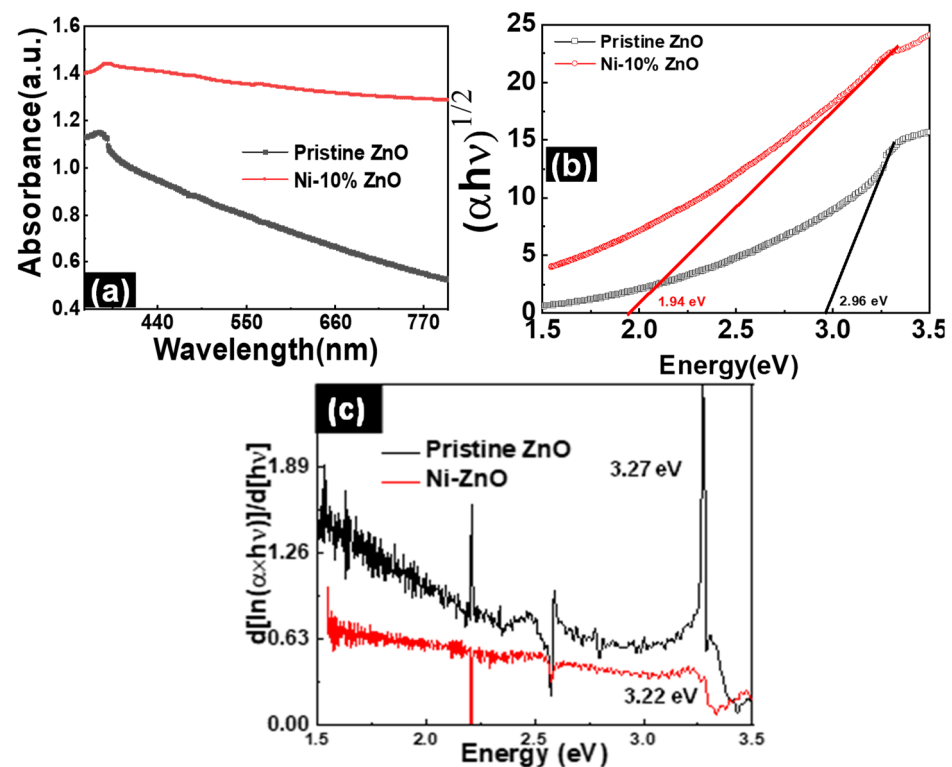


Figure 4. (a) UV–visible absorbance vs. wavelength spectra of pure and Ni-10%: ZnO thin films on a glass substrate. (b) Tauc plots for the spectra are shown in (a). (c) $\frac{d[\ln(\alpha h\nu)]}{d[h\nu]}$ vs. $h\nu$ plot for the pristine and doped ZnO NW film on the glass substrate.

The magnetization vs. magnetic field ($M-H$) curve measured at 300 K for the Ni-ZnO NWs is shown in Figure 5a. The magnetization saturates at almost ± 0.2 T, and there is a small hysteresis which is an indication of a soft ferromagnetic material. While pure ZnO NWs have been reported to be diamagnetic or weak ferromagnetic at room temperature, this weak ferromagnetism diminishes over time due to oxidation [11,31,32].

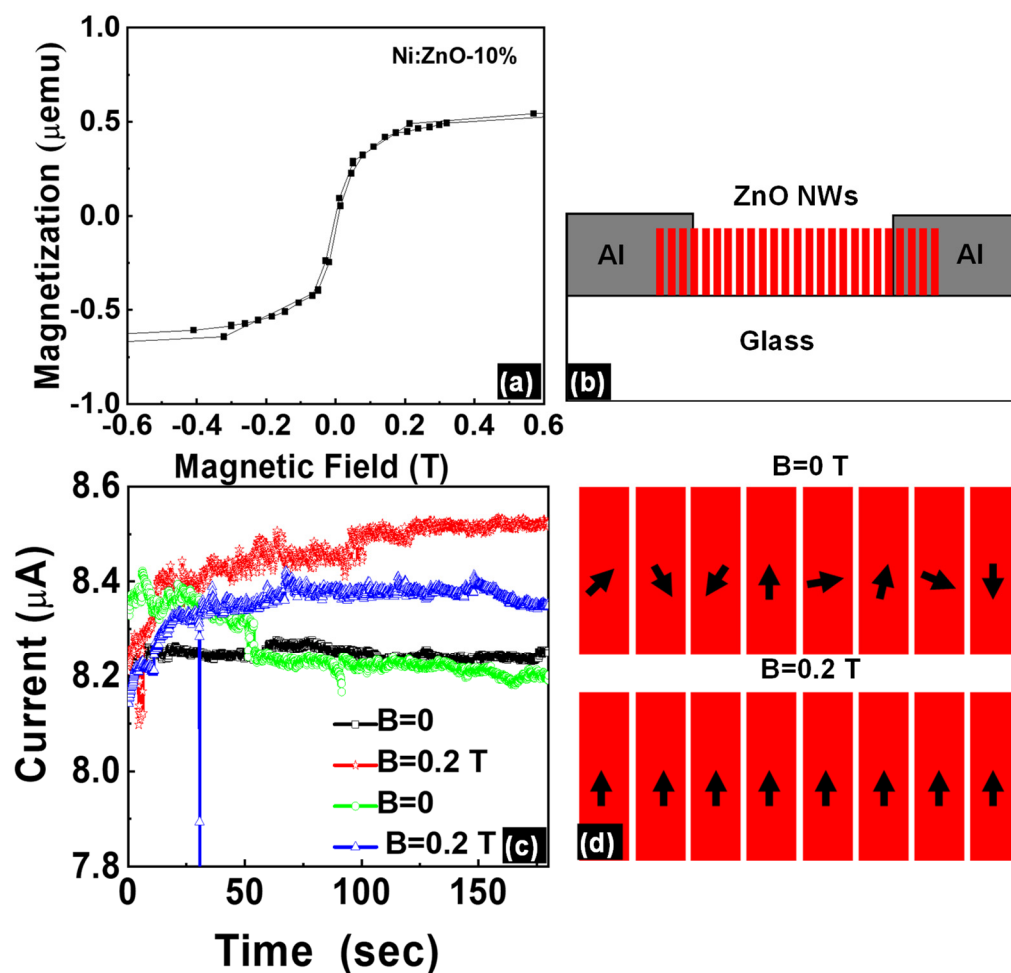


Figure 5. (a) Magnetization curve of a Ni-10%:ZnO NW film on a glass substrate, (b) schematic of the device used for the magneto transport measurements, (c) time versus current properties of the device shown in (b) with a fixed voltage bias and with and without a magnetic field, and (d) the schematic diagram showing the effect of the application of a field on the spin alignment.

The magneto-transport properties of a two-terminal device were measured using the computer-controlled Keithley 2400 source meter. The schematics of the device with a channel length of ~ 2 mm and width of ~ 7 mm is shown in Figure 5b. The NWs are vertically aligned and densely packed, as is evident from the SEM images, and the XRD spectra and the side walls of NWs are touching each other. Therefore, the current flow in this film will be a kind of tunneling current between adjacent NWs. Figure 5c is the transient current vs. time ($I-t$) properties of the device in dark conditions at a fixed bias voltage with and without an applied magnetic field. A permanent magnet (Nd-based magnet of ~ 0.2 T strength) was placed under the substrate with vertically aligned NWs grown on it, making an out-of-plane configuration. The length and width of the permanent magnet were kept smaller than the substrate to ensure a uniform magnetic field. The sample referred in Figure 5c is Ni-10% doped ZnO. B = 0 (black) is the case when there is no magnetic field applied while B = 0.2 T (red) is the first run in magnetic field. Then, we

turned off the magnetic field i.e., $B = 0$ (green), and turned it on again, the magnetic field i.e., $B = 0.2$ T (blue).

Usually, the time-dependent current in ZnO NW-based devices with a fixed voltage bias decreases in the air under ambient conditions due to the bias stress effect driven by oxidation on their surface [41]. As evident from Figure 5c, initially, the current remained almost constant without a magnetic field but decreased slowly with time due to ambient oxidation under the bias stress (see black curve). When applying a magnetic field, the current increased with time, as shown in Figure 5c blue curve.

We show a schematic diagram in Figure 5d to understand these results. In the absence of a magnetic field, spins are randomly oriented. When a magnetic field is applied, spins align along the direction of the applied magnetic field, and as a result, the scattering of charge carriers reduces. The increase in conductance is possibly due to crystal-field-split Ni 3d states lying close to the conduction band minima when they hybridize with the s/p states of the conduction/valence band [42,43]. Here the electrical contact of aluminum is nonmagnetic, so the magnetic field's effect is mainly the parallel alignment of electron spins in NWs, thus enhancing the carrier transmission in neighboring adjacent NWs [44].

Finally, the UV response of the two-terminal devices was studied under the illumination of a 395 nm UV LED ($8 \text{ mW}/\text{cm}^2$) with and without an applied magnetic field. The measured static I-V properties in linear and log scales are shown in Figure 6. Figure 6a is the linear scale IV properties of the Al/Ni-10% ZnO/Al two-terminal device in dark conditions and under the illumination of the UV LED with $B = 0$ and $B = 0.2$ T. This experiment was repeated twice. The response is increased with $B = 0.2$ T and is evident from the linear- and log-scale static IV properties shown in Figure 6a, and b. The photo-response of a photodetector strongly depends on the carrier mobility of the semiconducting material [41]. Here, the transport was enhanced in the case of a parallel alignment in the nanograins or nanowires, thus reducing the photo-carrier scattering and hence increasing photo-response. Recently, electrocatalysis and photocatalysis have been reported to be enhanced in metal oxides due to spin polarization [29]. The TiO_2 nanoparticle photocatalytic properties have been reported to be enhanced due to the defect-based spin polarization under the application of a magnetic field [45].

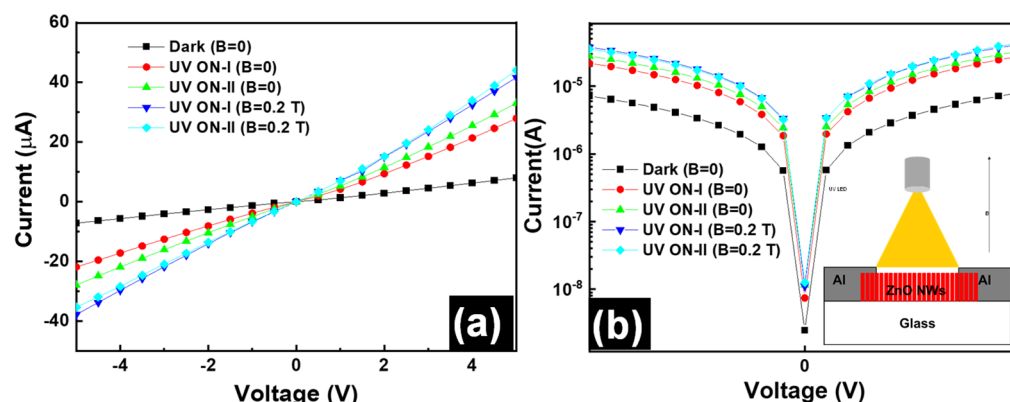


Figure 6. Static current–voltage properties of the two terminal ZnO nanowire film on glass with Al metal contacts in dark conditions and under the illumination of a UV LED; (a) linear scale and (b) log scale.

4. Conclusions

In conclusion, a Ni-doped ZnO NWs film was grown on a glass substrate. The XRD and SEM measurements revealed highly crystalline vertically aligned NWs, which were also supported by the microstructure analysis by transmission electron microscopy. The magnetic properties measured at 300 K showed a ferromagnetic response in the Ni-ZnO NWs. The transport properties of the film in dark conditions showed a negative magnetoresistive behavior, and the UV photo response was also observed to increase with the

magnetic field. This magneto transport and enhanced photo response were attributed to the alignment of spins resulting in a reduced carrier scattering. This will ultimately open an avenue for the next generation of spintronic and electronic devices.

Supplementary Materials: The following supporting information can be downloaded at: <https://www.mdpi.com/article/10.3390/magnetochemistry9080193/s1>, Figure S1: Stepwise schematic illustration of the growth of ZnO nanoparticles and Ni-ZnO nanowires on the glass substrate through a chemical solution route.

Author Contributions: Conceptualization, J.K. (Jamil Kazmi) and M.A.M.; methodology, J.K. (Jamil Kazmi), B.N. and R.A.S.K.; software, J.K. (Jamil Kazmi) and R.A.S.K.; validation, J.K. (Jamil Kazmi), S.R.A.R. and M.R.; formal analysis, J.K. (Jamil Kazmi), J.K. (Jamil Kazmi) and M.R.; investigation, S.R.A.R., J.K. (Jamil Kazmi), B.N. and M.R.; resources, S.R.A.R. and M.A.M.; data curation, J.K. (Jamil Kazmi); writing—original draft, J.K. (Jamil Kazmi); writing—review & editing, J.K. (Jamil Kazmi) and S.R.A.R.; supervision, S.R.A.R.; funding acquisition, M.A.M. All authors have read and agreed to the published version of the manuscript.

Funding: M.A.M acknowledges the financial support from the Ministry of Higher Education Malaysia through the Fundamental Research Grant Scheme, grant no. FRGS/1/2021/STG05/UKM/02/5.

Institutional Review Board Statement: Not applicable.

Informed Consent Statement: Not applicable.

Data Availability Statement: Not applicable.

Conflicts of Interest: The authors declare no conflict of interest.

References

1. Li, S.; Huang, M.; Lu, H.; McLaughlin, N.J.; Xiao, Y.; Zhou, J.; Fullerton, E.E.; Chen, H.; Wang, H.; Du, C.R. Nanoscale Magnetic Domains in Polycrystalline Mn₃Sn Films Imaged by a Scanning Single-Spin Magnetometer. *Nano Lett.* **2023**, *23*, 5326–5333. [[CrossRef](#)]
2. Redhu, P.; Kumar, S.; Kumar, A. Superconducting Proximity Effect and Spintronics. *Mater. Today Proc.* **2023**. [[CrossRef](#)]
3. Yang, A.J.; Wang, S.-X.; Xu, J.; Loh, X.J.; Zhu, Q.; Wang, X.R. Two-Dimensional Layered Materials Meet Perovskite Oxides: A Combination for High-Performance Electronic Devices. *ACS Nano* **2023**, *17*, 9748–9762. [[CrossRef](#)] [[PubMed](#)]
4. Al-Douri, Y.; Khan, M.M.; Jennings, J.R. Synthesis and Optical Properties of II–VI Semiconductor Quantum Dots: A Review. *J. Mater. Sci. Mater. Electron.* **2023**, *34*, 993. [[CrossRef](#)]
5. Ren, H.; Zhong, J.; Xiang, G. The Progress on Magnetic Material Thin Films Prepared Using Polymer-Assisted Deposition. *Molecules* **2023**, *28*, 5004. [[CrossRef](#)] [[PubMed](#)]
6. Sato, K.; Katayama-Yoshida, H. Electronic Structure and Ferromagnetism of Transition-Metal-Impurity-Doped Zinc Oxide. *Phys. B Condens. Matter* **2001**, *308–310*, 904–907. [[CrossRef](#)]
7. Dietl, T.; Ohno, H. Dilute Ferromagnetic Semiconductors: Physics and Spintronic Structures. *Rev. Mod. Phys.* **2014**, *86*, 187–251. [[CrossRef](#)]
8. Awschalom, D.D.; Flatté, M.E. Challenges for Semiconductor Spintronics. *Nat. Phys.* **2007**, *3*, 153–159. [[CrossRef](#)]
9. Ogale, S.B. Dilute Doping, Defects, and Ferromagnetism in Metal Oxide Systems. *Adv. Mater.* **2010**, *22*, 3125–3155. [[CrossRef](#)]
10. Kazmi, J.; Ooi, P.C.; Goh, B.T.; Lee, M.K.; Wee, M.F.M.R.; Karim, S.S.A.; Raza, S.; Raza, A.; Mohamed, M.A. RSC Advances Bi-Doping Improves the Magnetic Properties of Zinc Oxide Nanowires. *RSC Adv.* **2020**, *10*, 23297–23311. [[CrossRef](#)]
11. Kazmi, J.; Ooi, P.C.; Raza, S.R.A.; Boon Tong, G.; Karim, S.S.A.; Samat, M.H.; Lee, M.-K.; Razip Wee, M.F.M.; Taib, M.F.M.; Mohamed, M.A. Evidence of Room Temperature Ferromagnetism in Vertically Aligned Bi-Co Co-Doped ZnO Nanowires. *J. Phys. D. Appl. Phys.* **2021**, *54*, 415301. [[CrossRef](#)]
12. Ohno, Y.; Arata, I.; Matsukura, F.; Ohno, H.; Young, D.K.; Beschoten, B. Electrical spin injection in ferromagnetic/nonmagnetic semiconductor heterostructures. *Phys. E Low-Dimens. Syst. Nanostruct.* **2001**, *10*, 489–492. [[CrossRef](#)]
13. Joos, J.J.; der Heggen, D.; Amidani, L.; Seijo, L.; Barandiarán, Z. Elucidation of the Electron Transfer Mechanism in Eu²⁺ and Sm³⁺ Codoped CaF₂: A Step towards Better Understanding of Trapping and Detrapping in Luminescent Materials. *Phys. Rev. B* **2021**, *104*, L201108. [[CrossRef](#)]
14. Li, X.L.; Xu, X.H.; Quan, Z.Y.; Guo, J.F.; Wu, H.S.; Gehring, G.A. Role of Donor Defects in Enhancing Ferromagnetism of Cu-Doped ZnO Films. *J. Appl. Phys.* **2009**, *105*, 103914. [[CrossRef](#)]
15. Cho, Y.M.; Choo, W.K.; Kim, H.; Kim, D.; Ihm, Y. Effects of Rapid Thermal Annealing on the Ferromagnetic Properties of Sputtered Zn_{1-x}(Co_{0.5}Fe_{0.5})O Thin Films. *Appl. Phys. Lett.* **2002**, *80*, 3358–3360. [[CrossRef](#)]
16. Tong, L.N.; Cheng, T.; Han, H.B.; Hu, J.L.; He, X.M.; Tong, Y.; Schneider, C.M. Photoluminescence Studies on Structural Defects and Room Temperature Ferromagnetism in Ni and Ni-H Doped ZnO Nanoparticles. *J. Appl. Phys.* **2010**, *108*, 023906. [[CrossRef](#)]

17. Wakano, T.; Fujimura, N.; Morinaga, Y.; Abe, N.; Ashida, A.; Ito, T. Magnetic and Magneto-Transport Properties of ZnO: Ni Films. *Phys. E Low-Dimens. Syst. Nanostruct.* **2001**, *10*, 260–264. [[CrossRef](#)]
18. Singh, S.; Rama, N.; Rao, M.S.R. Influence of D-d Transition Bands on Electrical Resistivity in Ni Doped Polycrystalline ZnO. *Appl. Phys. Lett.* **2006**, *88*, 222111. [[CrossRef](#)]
19. Cui, J.B.; Gibson, U.J. Electrodeposition and Room Temperature Ferromagnetic Anisotropy of Co and Ni-Doped ZnO Nanowire Arrays. *Appl. Phys. Lett.* **2005**, *87*, 133108. [[CrossRef](#)]
20. Orek, C.; Keser, S.; Kaygili, O.; Zuchowski, P.; Bulut, N. Structures and Optical Properties of Zinc Oxide Nanoclusters: A Combined Experimental and Theoretical Approach. *J. Mol. Model.* **2023**, *29*, 227. [[CrossRef](#)] [[PubMed](#)]
21. Morales-Mendoza, J.E.; Herrera-Pérez, G.; Fuentes-Cobas, L.; Hermida-Montero, L.A.; Pariona, N.; Paraguay-Delgado, F. Synthesis, Structural and Optical Properties of Cu Doped ZnO and CuO–ZnO Composite Nanoparticles. *Nano-Struct. Nano-Objects* **2023**, *34*, 100967. [[CrossRef](#)]
22. Potera, P.; Virt, I.S.; Cieniek, B. Structure and Optical Properties of Transparent Cobalt-Doped ZnO Thin Layers. *Appl. Sci.* **2023**, *13*, 2701. [[CrossRef](#)]
23. Sharma, A.; Kumar, P. Review on Structural, Magnetic, Optical Properties of Manganese Doped Zinc Oxide Nanoparticles. *Mater. Today Proc.* **2023**. [[CrossRef](#)]
24. Guermat, N.; Daranfed, W.; Bouchama, I.; Bouarissa, N. Investigation of Structural, Morphological, Optical and Electrical Properties of Co/Ni Co-Doped ZnO Thin Films. *J. Mol. Struct.* **2021**, *1225*, 129134. [[CrossRef](#)]
25. Tiwari, C.; Pandey, A.; Dixit, A. Precursor Mediated and Defect Engineered ZnO Nanostructures Using Thermal Chemical Vapor Deposition for Green Light Emission. *Thin Solid Films* **2022**, *762*, 139539. [[CrossRef](#)]
26. Soumya, C.; Pradyumnan, P.P. Enhancement of Thermoelectric Properties of Transition Metals, Nickel and Copper Dually Doped ZnO. *Mater. Today Commun.* **2023**, *35*, 106197. [[CrossRef](#)]
27. Benhaliliba, M. ZnO a Multifunctional Material: Physical Properties, Spectroscopic Ellipsometry and Surface Examination. *Optik* **2021**, *241*, 167197. [[CrossRef](#)]
28. Javed, M.; Khan, A.A.; Khisro, S.N.; Majeed, A.; Kazmi, J.; Bilkees, R.; Hussain, M.; Mohamed, M.A. Charge Conduction Mechanism and Non-Debye Type Relaxation in LaCrO₃ Perovskite Orthochromite. *Mater. Chem. Phys.* **2022**, *290*, 126522. [[CrossRef](#)]
29. Li, Y.; Wang, T.; Asim, M.; Pan, L.; Zhang, R.; Huang, Z.F.; Chen, Z.; Shi, C.; Zhang, X.; Zou, J.J. Manipulating Spin Polarization of Defected Co₃O₄ for Highly Efficient Electrocatalysis. *Trans. Tianjin Univ.* **2022**, *28*, 163–173. [[CrossRef](#)]
30. Huang, M.H.; Mao, S.; Feick, H.; Yan, H.; Wu, Y.; Kind, H.; Weber, E.; Russo, R.; Yang, P. Room-Temperature Ultraviolet Nanowire Nanolasers. *Science* **2001**, *292*, 1897–1899. [[CrossRef](#)]
31. Kazmi, J.; Ooi, P.C.; Raza, S.R.A.; Goh, B.T.; Karim, S.S.A.; Samat, M.H.; Lee, M.K.; Mohd. Razip Wee, M.F.; Taib, M.F.M.; Mohamed, M.A. Appealing Stable Room-Temperature Ferromagnetism by Well-Aligned 1D Co-Doped Zinc Oxide Nanowires. *J. Alloys Compd.* **2021**, *872*, 159741. [[CrossRef](#)]
32. Kazmi, J.; Raza, S.R.A.; Ahmad, W.; Masood, A.; Jalil, A.; Mohd Raub, A.A.; Abbas, A.; Rafiq, M.K.S.; Mohamed, M.A. Free Carrier-Mediated Ferromagnetism in Nonmagnetic Ion (Bi-Li) Codoped ZnO Nanowires. *Phys. Chem. Chem. Phys.* **2023**, *25*, 14206–14218. [[CrossRef](#)]
33. Saeed Khan, R.A.; Kazmi, J.; Ansari, B.; Raza, S.R.A.; Tabbasum, N.; Mohamed, M.A.; Kazmi, J.; Hassan, Z.U.; Ahmed, M.N.; Majeed, A.; et al. N-Pentylisatin and ZnO NWs Based Organic-Inorganic Hybrid Device for Broad Range Photodetection. *Mater. Chem. Phys.* **2022**, *281*, 125919. [[CrossRef](#)]
34. Raub, A.A.M.; Yunas, J.; Mohamed, M.A.; Kazmi, J.; Ridwan, J.; Hamzah, A.A. Statistical Optimization of Zinc Oxide Nanorod Synthesis for Photocatalytic Degradation of Methylene Blue. *Sains Malays.* **2022**, *51*, 1933–1944. [[CrossRef](#)]
35. Raub, A.A.M.; Yunas, J.; Mohamed, M.A.; Kazmi, J.; Ridwan, J. Structural and Optical Properties Investigation of Graphene Oxide Coated ZnO Nanorods for Enhanced Photocatalytic Effect. In Proceedings of the 2021 IEEE Regional Symposium on Micro and Nanoelectronics (RSM), Kuala Lumpur, Malaysia, 2–4 August 2021; pp. 104–107. [[CrossRef](#)]
36. Javed, M.; Khan, A.A.; Khan, M.N.; Kazmi, J.; Mohamed, M.A. Investigation on Non-Debye Type Relaxation and Polaronic Conduction Mechanism in ZnCr₂O₄ Ternary Spinel Oxide. *Mater. Sci. Eng. B* **2021**, *269*, 115168. [[CrossRef](#)]
37. Mahmud, M.A.; Elumalai, N.K.; Upama, M.B.; Wang, D.; Soufiani, A.M.; Wright, M.; Xu, C.; Haque, F.; Uddin, A. Solution-Processed Lithium-Doped ZnO Electron Transport Layer for Efficient Triple Cation (Rb, Ma, Fa) Perovskite Solar Cells. *ACS Appl. Mater. Interfaces* **2017**, *9*, 33840–33854. [[CrossRef](#)] [[PubMed](#)]
38. Shin, S.; Kim, Y.; Lee, M.H.; Jung, J.; Seol, J.H.; Nah, J. Lithium-Doped Zinc Oxide Nanowires À Polymer Composite for High Performance Flexible Piezoelectric Nanogenerator. *ACS Nano* **2014**, *8*, 10844–10850. [[CrossRef](#)] [[PubMed](#)]
39. Lee, E.C.; Chang, K.J. P-Type Doping with Group-I Elements and Hydrogenation Effect in ZnO. *Phys. B Condens. Matter* **2006**, *376–377*, 707–710. [[CrossRef](#)]
40. Tuoc, V.N.; Huan, T.D.; Lien, T.H. Le Impact of Surface on the D0 Ferromagnetism of Lithium-Doped Zinc Oxide Nanowires. *IEEE Trans. Magn.* **2014**, *50*, 2400407. [[CrossRef](#)]
41. Paquin, F.; Rivnay, J.; Salleo, A.; Stingelin, N.; Silva, C. Multi-Phase Semicrystalline Microstructures Drive Exciton Dissociation in Neat Plastic Semiconductors. *J. Mater. Chem. C* **2015**, *3*, 10715–10722. [[CrossRef](#)]
42. Hirohata, A.; Yamada, K.; Nakatani, Y.; Prejbeanu, L.; Diény, B.; Pirro, P.; Hillebrands, B. Review on Spintronics: Principles and Device Applications. *J. Magn. Magn. Mater.* **2020**, *509*, 166711. [[CrossRef](#)]

43. Baibich, M.N.; Broto, J.M.; Fert, A.; Van Dau, F.N.; Petroff, F.; Eitenne, P.; Creuzet, G.; Friederich, A.; Chazelas, J. Giant Magnetoresistance of (001)Fe/(001)Cr Magnetic Superlattices. *Phys. Rev. Lett.* **1988**, *61*, 2472–2475. [[CrossRef](#)] [[PubMed](#)]
44. Singh, S.; Rao, M.S.R. Optical and Electrical Resistivity Studies of Isovalent and Aliovalent 3d Transition Metal Ion Doped ZnO. *Phys. Rev. B-Condens. Matter Mater. Phys.* **2009**, *80*, 045210. [[CrossRef](#)]
45. Pan, L.; Ai, M.; Huang, C.; Yin, L.; Liu, X.; Zhang, R.; Wang, S.; Jiang, Z.; Zhang, X.; Zou, J.J.; et al. Manipulating Spin Polarization of Titanium Dioxide for Efficient Photocatalysis. *Nat. Commun.* **2020**, *11*, 418. [[CrossRef](#)] [[PubMed](#)]

Disclaimer/Publisher’s Note: The statements, opinions and data contained in all publications are solely those of the individual author(s) and contributor(s) and not of MDPI and/or the editor(s). MDPI and/or the editor(s) disclaim responsibility for any injury to people or property resulting from any ideas, methods, instructions or products referred to in the content.